

Pre-doped oxygenated defects activate nitrogen-doped graphene for the oxygen reduction reaction

Lin Jiang

Leiden University

Bas van Dijk

Leiden University

Longfei Wu

Eindhoven University of Technology

Clement Maheu

Technische Universität Darmstadt

Jan Hofmann

Technical University of Darmstadt <https://orcid.org/0000-0002-5765-1096>

Viorica Tudor

Leiden University

Marc Koper

Leiden Institute of Chemistry, Leiden University

Dennis Hetterscheid

Leiden University

Gregory Schneider (✉ g.f.schneider@chem.leidenuniv.nl)

Leiden University <https://orcid.org/0000-0002-3156-4525>

Article

Keywords: chemical dopants, metal-free carbon materials, Pre-doped oxygenated defects, nitrogen-doped graphene, oxygen reduction reaction

Posted Date: May 7th, 2021

DOI: <https://doi.org/10.21203/rs.3.rs-479206/v1>

License:   This work is licensed under a Creative Commons Attribution 4.0 International License.

[Read Full License](#)

Abstract

The presence of defects and chemical dopants in metal-free carbon materials plays important roles in the electrocatalysis of the oxygen reduction reaction (ORR). The precise control and design of defects and dopants in carbon electrodes will allow the fundamental understanding of activity-structure correlations for tailoring catalytic performance of carbon-based, most particularly graphene-based electrode materials. Herein, we adopted monolayer graphene – a model carbon-based electrode – for systematical introduction of nitrogen and oxygen dopants, together with vacancy defects, and studied their roles in catalyzing ORR. Compared to pristine graphene, nitrogen doping exhibited a limited effect on ORR activity. In contrast, nitrogen doping in graphene pre-doped with vacancy defects or oxygen enhanced the activities by 3.7 and 6.8 times, respectively. The optimal activity was achieved for nitrogen doping in graphene functionalized with oxygenated defects – 4.6 times more than nitrogen-doped and 7.3 times more than pristine graphene. More importantly, oxygenated defects is highly related to the $4e^-$ pathway instead of nitrogen dopants. This work indicates a non-negligible contribution of oxygen and especially oxygenated vacancy defects for the catalytic activity of nitrogen doped graphene.

Introduction

Nitrogen-doped (N-doped) carbon-based metal-free materials like graphene and carbon nanotubes are effective and promising alternatives to platinum catalysts for the oxygen reduction reaction (ORR), a critical reaction for renewable energy technologies in fuel cells.^{1,2,3,4} A tremendous amount of experimental and theoretical efforts have been devoted to determine the active sites of N-doped carbon materials for the ORR.^{5,6,7} Nitrogen dopants in graphitic carbon materials, either pyridinic N^{6,8} or graphitic N⁹, have been proposed to be potential active sites for ORR. Particularly, positively charged carbon atoms next to pyridinic nitrogen atoms in graphite have been suggested to preferentially adsorb O₂ molecules and thus favor fast ORR kinetics in acidic medium.^{8,10} In contrast, pyridinic N-doped graphene is not ORR active.^{6,11,12} On the other hand, a range of carbon defects and oxygen functional groups in carbon have exhibited intriguing performance in catalyzing ORR.^{13,14} For example, edged pentagon carbon defects are more active towards the ORR than N dopants in graphitic systems.^{12,15} In part, the controversy of active sites for ORR in N-doped graphene can be ascribed to the significant variations in structure and morphology of the studied materials, i.e. graphene nanoflakes dispersions composed of multilayered nanosheets containing abundant oxygen groups, edges and carbon defects.^{16,17} Typically the inhomogeneous active sites for ORR catalysis, caused by flake aggregation, irreversible pyrolysis or vigorous chemical treatments, are less considered. Hence, it is of pivotal importance to systematically disentangle every element in graphitic system that is susceptible to contribute to the ORR activity.

In carbon materials, the origin of the catalytic activities resides in the electronic structure, which can be modulated by chemical doping and structure engineering.¹⁸ Especially, when a carbon system is functionalized with multiple components – multilayered sheets in different size and crystallinity,

heteroatom doping and atomic defects – alternating the electronic structure, each can contribute individually and synergistically to catalysis. For example, trace amounts of heteroatoms doping like nitrogen are reported to significantly boost the ORR activity of a defective graphene by tuning the electronic structure of the pentagon defects functioning as the active sites.¹⁹ In addition, a theoretical study describing proton-coupled electron transfer on graphene surfaces showed that carbene type active sites are stabilized by a combination of pyridinic nitrogen and quinone type oxygen functionalities.²⁰ Especially, oxygen groups are abundant in graphene nanoflakes and other carbon materials due to their high oxygen affinity. However, little experimental attention has been given to distinguish the individual roles of oxygen functionalities and carbon defects within N-doped carbon systems for ORR. The absence of a suitable model carbon catalyst with a well-controlled chemical composition and atomic structure has been the key limiting factor.

In this study, a graphene monolayer grown via the chemical vapor deposition (CVD) method was chosen as a model catalyst since it provides a reliable and well-defined sp^2 hybridized carbon surface.^{21, 22, 23} Such a well-defined model catalyst is desired to disentangle the relationship between ORR activity and the atomic carbon structure upon heteroatom doping and carbon defects, all-in-all for the rational design of more efficient carbon catalysts. Here, the two sides of one graphene (G) surface – designated to be pristine G supported on a polymer and graphene on a glassy carbon electrode (G@GC) in a disk-ring electrode system – demonstrate contrast ORR activity upon identical nitrogen doping treatments owing to the intrinsic difference in the surface oxygen-containing groups. Further on, nitrogen, oxygen and vacancy defects were introduced into graphene in single-, dual- and triple-doping modes, respectively. It is found that single-doped nitrogen in graphene has a limited effect on the ORR while a synergy effect of nitrogen with oxygen and/or defects enhances the activity remarkably. Especially, the highest activities achieved on the optimized triple-doped samples suggests a critical role of oxygenated defects in facilitating the ORR activity of N-doped graphene. Moreover, the presence of nitrogen dopants in the functionalized carbon system is essential to boost the activity owing to their impacts on the electronic structure.

Results And Discussion

Structural characterization of N-doped graphene

Nitrogen dopants were systematically introduced into the basal plane of a monolayer graphene upon ammonia plasma treatments (Details can be found in Supplementary Information). Raman spectroscopy, electron microscopy and transport characterization were performed to reveal the impact of nitrogen dopants on the atomic and electronic structure of monolayer graphene. Raman spectroscopy (Figure 1a) was conducted to evaluate the N-doping process on chemical vapor deposition (CVD) graphene supported by a SiO_2/Si substrate. For pristine graphene, two main characteristic peaks for monolayer graphene can be found. The G peak ($\sim 1580\text{ cm}^{-1}$) arises from the C-C stretching within all sp^2 carbon systems. As the overtone of the breathing modes of six-atom rings, the sharp 2D peak ($\sim 2670\text{ cm}^{-1}$) is

sensitive to the number of graphene layers and doping effects.²⁴ The monolayer crystallinity was also reflected in the high resolution transmission electron microscopy (HRTEM) images and the fast Fourier transform (FFT) pattern in Figure S1. After more than 2 s of nitrogenation, a D peak appears at $\sim 1340 \text{ cm}^{-1}$ (see Figure 1a) that corresponds to single phonon intervalley scattering events and is associated with the defects induced by the incorporation of nitrogen atoms into the lattice of graphene (i.e., nitrogen dopants and the edge defects).²⁵ Upon longer nitrogenation times ($t_N > 6 \text{ s}$), a D' peak at 1620 emerges as a shoulder of the G peak due to the intervalley scattering induced by defects.²⁶ When the t_N increases from 0 to 60 s, the intensity ratio $I(2D)/I(G)$ decreases from 2.0 to 0.7 (Figure 1b) and the 2D peak shifts from 2674 to 2665 (Figure S2a), both are in line with an electron (n-) doping effect in nitrogenated graphene.^{27, 28, 29} As a quantitative reflection of the defect density (ρ) and interdefect distance (λ),³⁰ the ratio of $I(D)/I(G)$ in Figure 1c (black line) exhibits a similar growth trend with the peak widths (see ρ and λ in Table S1). Such consistent saturation trends may correspond to the clustering of nitrogen dopants at high doping level.^{11, 31} This is reflected by a domain-like defect distribution in graphene after 30 s of nitrogenation (Figure 1d). The full width at half maximum values (FWHM) for the D, G and 2D peaks (Figure S2b) slightly increase upon increasing t_N from 0 to 30 s and saturate at 60 s. The increase of the FWHMs indicates a growth of defect density. Specifically, the increasing trends for both the $I(D)/I(G)$ ratio and the FWHM of the G peak confirm the dominance of sp^2 -hybridized carbon network over the introduced defects, thus we conclude that the N-doped graphene still has a high lattice integrity. It is reported that a ratio of circa 3 for $I(D)/I(D')$ represents boundary defects while a ratio of circa 7 indicates vacancy defects as based on a model of uniform defect distribution without clustering.³² In our case, the $I(D)/I(D')$ ratios vary from 6.5 (10-20 s of nitrogenation) to 5 (more than 30 s of nitrogenation) (Figure 1c, blue dots) indicating that nitrogen dopants behave more like vacancy defects. To conclude, Raman spectroscopy shows that N-doped graphene has a high, uniform graphitization level and vacancy-like N dopants.

Next, we studied the electron transport characteristics of graphene in the configuration of an electrochemically-gated graphene field effect transistor (GFET) that was fabricated following a previously reported strategy (see Supplementary Information).³³ We used an epoxy substrate to support a clean, pristine graphene surface that was protected by a clean and annealed copper substrate (Figure 1e). Moreover, this graphene surface was never in contact with and thus contaminated by any polymer that is generally used for graphene transfer,³⁴ and was only exposed to the ambient oxygen in a short period (within 24 to 48 hrs) before measurements. Our previous work has confirmed that this graphene surface contains a lower density of charged impurities (i.e. originating from ambient oxidation or trapped impurities) than polymer transferred one.³³ The conductance (G) of this clean graphene in Figure 1f (black line) demonstrates an ambipolar behavior with respect to the gate voltage (V_g). The $G(V_g)$ curves start to shift negatively after 10 s of nitrogenation and the charge neutrality point (CNP) shifts by -30 to -60 mV between 20 to 60 s of nitrogenation. Such shifts suggest an n-doping effect in graphene (Figure 1g). Using the capacitor model in the electrochemical-gating configuration,³⁵ we extract the carrier mobility (μ) of graphene, which decreases from $\sim 3800 \text{ cm}^2 \text{ V}^{-1} \text{ s}^{-1}$ to $\sim 550 \text{ cm}^2 \text{ V}^{-1} \text{ s}^{-1}$ after 30 s of nitrogenation and

subsequently levels off at 60 s of nitrogenation (Figure 1g, black). Notably, the high carrier mobility value for pristine graphene confirms its intrinsic high-quality and less charge impurities. Consistent with the saturation trend of $I(D)/I(G)$ ratios in Figure 1c, the evolution of graphene carrier mobility is predicted to be closely related to the distribution of nitrogen dopants. At low doping levels ($t_N < 30$ s), nitrogen dopants independently implant into the carbon lattice, resulting in a rapid and dramatic conductivity degradation of graphene. At high doping levels ($30 < t_N < 60$ s), nitrogen dopants form clusters around the pre-existing nitrogen doping sites, resulting in a lower conductivity degradation of graphene. These observations reveal that nitrogen dopants in the monolayer graphene lattice cause significant intervalley scattering, reduce the carrier mobility and conductivity, and induce an n-doping effect.

Graphene surface preparation for ORR

CVD graphene supported on the as-grown copper foil intuitively has two faces: one facing to the copper foil (copper-face) and the other facing to the air (air-face) (Figure 2a). As mentioned above, the copper-face of graphene – that has been previously confirmed to contain minimized impurities (i.e. oxidation, contaminations)³³ – was adopted for the transport measurement (Figure 1e). To prepare monolayer graphene electrodes for ORR, both faces were employed according to the measurement configurations. In details, the copper-face was transferred onto the epoxy support (similar to the GFET device preparation), referred to as pristine G (Figure 2b); while the air-face was transferred onto glassy carbon (GC) electrode using a polymer,³⁴ referred to as G@GC (Figure 2c and Figure S3). The slight differences in the original surface chemistry of the two graphene electrodes significantly determine their catalytic performance upon nitrogenation, which will be discussed further.

X-ray photoelectron spectroscopy (XPS) was used to characterize the chemical structure of nitrogenated graphene. Figure 2d shows the XPS N 1s (b) spectra for pristine, 30 s and 60 s of N-doped graphene. The N 1s spectra for 30 s N-doped samples consist of two main peaks centered at 398.9 eV and 399.9 eV, corresponding to pyridinic (pyrid-) and pyrrolic (pyrro-) N.^{12, 36} For 60 s N-doped graphene, in addition to the pyrid- and pyrro-N peaks, another peak at 401.1 eV is observed and assigned to graphitic (graph-) N. Correspondingly, the XPS C 1s spectra for pristine graphene, 30 s and 60 s N-doped graphene is shown in Figure S4. The N/C and O/C ratio increases respectively from 2.0% and 9.0% for 30 s to 3.1% and 21% for 60 s of nitrogenation. Moreover, the dominant forms of pyrid- and pyrro-N agree well with the observed n-type doping effect in Figure 1.^{37, 38}

The ORR activity was first studied with pristine G supported on the epoxy substrate for both acid and alkaline media. Figure S5a-b shows the cyclic voltammograms (CVs) of pristine G in 0.1 M H₂SO₄ and 0.1 M NaOH solution saturated with Ar and O₂ respectively in a stationary configuration. A more positive onset potential in alkaline medium (~0.68 V) than in acidic medium (~0 V), and a higher current density (~4-fold at -0.2 V) in 0.1 M NaOH shows the higher ORR activity in alkaline medium. It is well known that carbon-based catalyst are more active for the ORR in alkaline media. This is most likely due to being the

first intermediate in the mechanism of ORR, which is formed by an electron transfer reaction that is not coupled to proton transfer and therefore does not scale linearly with the RHE reference scale.³⁹

The LSV curves in alkaline medium have an extra reduction peak at ca. 0.45 V. This peak is ascribed to oxygen reduction catalyzed by the oxygen-containing groups present on the surface of graphene and other carbon electrodes including glassy carbon.⁴⁰ In addition, more aged pristine G showed increased current in this region (Figure S5c). Therefore, only graphene samples producing similar low peak currents at 0.45 V with the LSV in Figure 3a are used for doping treatment studies. Upon nitrogen doping from 0 to 60 s, the catalytic current densities are observed to decrease monotonically both in acidic (Figure 2e) and in alkaline medium (Figure 2f). It differs from earlier reports claiming that n-doping of nitrogenated graphene improves ORR activity by creating Lewis basic sites which enhance initial O₂ adsorption.^{5, 8} In our case, the observed decrease in ORR activity of graphene after nitrogenation suggests that the N-doping sites within the graphene surface do not contribute to the generation of active catalytic sites. Such an observation is supported by recent reports that the catalytic activity of graphene decreases upon nitrogenation.^{11, 12} For example, N-doped graphene was reported to show similar ORR activity with pristine graphene.¹² A theoretical study proposes that the nitrogen atoms in N-doped graphene could actually hinder the adsorption of oxygen molecules onto the graphene surface due to their higher electron density.⁴¹

Further on, the air-face of CVD graphene as the opposite face of pristine G was transferred onto the GC disk electrode, which is part of the rotating ring-disk electrode (RRDE). Two types of graphene samples on GC support were prepared (Figure S3) and compared for their ORR performance (Figure S6a,c). A monolayer graphene on the GC disk (denoted as G'@GC) decreases the ORR current compared to that of bare GC, indicating that fewer active sites are available on the graphene surface (Figure S6a). Furthermore, bilayer graphene on GC (namely the G@GC) has an even more reduced ORR current compared to the G'@GC. This implies that the GC as the underlying substrate has a certain influence on the catalysis of the graphene overlayer, for instance through cracks in this monolayer graphene film. In contrast, the G@GC displays reliable reproducibility and reliability reflected by LSV curves and Raman spectra (see Figure S6b-d and Supplementary Note 2.3) before and after rotation tests. Therefore, the G@GC was used for the RRDE measurements (*vide infra*). Compared to the LSV of pristine G, G@GC (at 0 rpm) has a more pronounced peak at 0.45 V (Figure 2g). As previously described, this feature is probably related to a higher surface oxidation of G@GC as compared to pristine G. Of note, G@GC exhibits a slightly increased current after 30 s of nitrogenation and significantly boosted activity after 60s of nitrogenation, which is in high contrast to that on pristine G (Figure 2h). Given the decrease of conductivity versus the increase of ORR activity upon nitrogen doping, it is concluded that the conductivity of the graphene upon the employed doping conditions ($\sim 600 \text{ cm}^2 \text{ V}^{-1} \text{ s}^{-1}$ for 30 to 60 s of nitrogen doping) is not necessarily the limiting factor for ORR catalysis.

Such contrasts in ORR activity between the two faces of the same monolayer graphene can be attributed to the different surface chemistry and underlying substrates between pristine G and G@GC. For the

substrates, the GC electrode can only contribute to ORR of G@GC if cracks or holes were introduced during transfer process. To test this possibility, the ORR currents of G@GC after 60 s of nitrogenation (N60), partially exposed GC electrodes (from 10% to 50% in terms of area) and a fully exposed bare GC were compared (Figure S7). Due to the large amounts of carbon defects and oxygen functionalities, bare GC exhibits a distinct polarization curve with a prominent extra peak at ca. 0.45 V. In contrast, N60 exhibits a much larger ORR current at a high overpotential (~ 0.2 V vs RHE) and a relatively lower current at 0.45 V compared to all partially exposed GC electrodes. Such a contrast indicates that the underlying GC substrate plays a negligible role in the ORR activity of N60. Therefore, the surface chemistry of graphene upon nitrogenation should be mainly responsible for the observed contrast in ORR activity. As confirmed by XPS (Figure 2d and Figure S4) and the ORR performance (Figure 2h), surface-containing oxygen groups are expected to play a critical role to boost the catalytic properties of graphene upon N-doping. Inspired by the recent work that oxygen-containing groups^{5,8} and carbon defects^{15,19,42} in carbon-based materials are closely related to the active ORR performance, we further investigate the activities of graphene doped or co-doped with nitrogen, oxygen as well as vacancy defects, which can intrinsically or unintentionally present in carbon materials.

Activity correlations in activated N-doped Graphene

We used a rotating ring-disk electrode (RRDE) method to gain insights into the ORR kinetics and activity of nitrogenated graphene. The current was measured at both the glassy carbon (GC) disk and the platinum ring. The Pt ring was held at a potential of 1.2 V, to oxidize ORR products such as hydrogen peroxide (the form of H_2O_2 in alkaline medium) and/or superoxide. G@GC was continued for individual and cooperative doping of nitrogen (30 s nitrogenation, N30), vacancy defects (30 s argon plasma, Ar30) and oxygen (10 s oxygenation, O10) to compare their synergy effect on ORR. The doping levels for N30, Ar30 and O10 were controlled using comparable defect densities reflected by Raman spectra (Figure S8). The dual-doping and triple-doping graphene samples were simply denoted, for example, as O-N (O10 followed by N30) and Ar-O-N (Ar30 followed by O10 and lastly N30), respectively. In particular, the original G@GC without any doping treatment was simplified as G.

Furthermore, ORR activities are evaluated based on the stable catalytic currents obtained at potentials where the diffusion limited condition is achieved. Accordingly, the LSV curves collected at rotation speed ranging from 400 rpm to 1000 rpm in Figure S9 show that ORR currents for most of the graphene samples reach the stability between -0.2 to 0 V. Therefore, currents at 0 V vs RHE are summarized for activity comparison. The LSV curves in Figure 3a show that N30 exhibits a similar current with G (~ 1.6 -fold increase), indicating a limited effect of N-doping alone in the graphitic surface on ORR. In contrast, Ar30 and O10 with similar doping densities with N30 enhance the activity by ~ 3.2 and ~ 3.8 folds, respectively. O10 also shows a higher onset potential of 0.63 V comparing with G at ~ 0.5 V. Such contrasts suggest that vacancy defects and oxygen dopants are more ORR active than nitrogen dopants in graphene. The co-doped configurations shown in Figure 3b, Ar-N and O-N show much-enhanced activity (~ 3.7 and ~ 6.8 -fold increase, respectively) than N30 alone, while Ar-O-N plateaus the activity up to ~ 7.3 -folds of G with the largest onset potential of 0.7 V. Importantly, the significant activity

enhancement in Ar-O-N compared to other single or dual doping samples (N30, Ar-N, O-N) indicates the activation roles of oxygenation and vacancy defects for N-doped graphene with enhanced ORR activity. Further control tests in Figure 3c show that Ar-O and O-Ar exhibit similar currents with their single doped counterparts (namely Ar30 and O10), suggesting the essential catalytic role of N-dopants or the nitrogenation process creating the active sites in graphene to boost ORR.

Given the evident synergistic effect from N, O dopants and vacancy defects in dual- and triple-doped graphene, we particularly focused on the comparison of chemical compositions for Ar-N, O-N and Ar-O-N and the correlation with their ORR activities. XPS C1s and N1s spectra for Ar-N, O-N and Ar-O-N are displayed in Figure 3d-e. The C1s spectra can be deconvoluted into five peaks: sp^2 C-C (284.4 eV), sp^3 C-C (285.0 eV), C-O/C=N (286.4 eV), C=O/C-N (288.0 eV), and O-C=O (289.0 eV), respectively.^{36, 43} In addition to the dominant sp^2 C, Ar-O-N contains the highest C=O/C-N content (6.7 %) while Ar-N has the most sp^3 C content (17.8 %). As shown in N1s spectra, the three typical N dopants, namely pyrid-N (398.9 eV), pyrro-N (399.9 eV) and graph-N (401.1 eV), exist in all the three samples. The highest atom % for pyridinic N, pyrrolic N and graphitic N is found respectively in O-N (1.1), Ar-O-N (3.5) and Ar-N (0.6). In addition, XPS characterizations were also conducted for other single-doped (Ar30, O10) and dual-doped (Ar-O) samples (Figure S10) for comparison.

To gain a deep understanding of the origin of the enhanced activity, we further investigated the relations between chemical composition and catalytic performance. Derived from the LSV data in Figure 3a-c, ORR activities rank from low to high in the order of non-doped G, single-doped N30 and Ar30 dual-doped Ar-O, single-doped O10, and dual- and triple-doped Ar-N, O-N and Ar-O-N in Figure 3f. After analyzing the atom % of different functionalities in graphene samples (see Table S2), the sum contents of carbon-oxygen (C-O%) and nitrogen (N%) are found to be positively correlated to ORR activities of graphene after excluding the high-proportional contributions of C=O and O-C=O groups in O10 and Ar-O. Oxygenation as the final doping treatment (i.e. Ar-O and O10) results in relatively higher carbon-oxygen atom % (~20) in graphene, which are in high contrast to non-oxygenated samples (~8.6-9.9 for G, N30, Ar30) and oxygenated samples followed by nitrogenation (~12.6-13.3 for O-N and Ar-O-N). Specifically, the higher N atom % in dual-doped samples (O-N, Ar-N) comparing with N30 suggest that oxygenated groups in graphene can enhance the doping levels of the following nitrogenation. In addition, the N-doped graphene samples (Ar-O-N, O-N and Ar-N) generally contain lower oxygen contents but much higher ORR activity than the non-nitrogenated graphene (Ar-O and O10), suggesting that relatively low atomic ratios of oxygen groups in graphene are sufficient to activate the ORR activity of N-doped graphene. Also, the presence of N dopants in N-doped samples versus the non-N-doped counterparts (i.e. N30 vs G, Ar-N vs Ar-O, O-N vs O, Ar-O-N vs O-N) further confirm the critical contribution of N-dopants for ORR (Table S2). But the similar N atom % for Ar-N (~4.4), O-N (~4.4) and Ar-O-N (~4.5) samples also suggests that ORR activity is not purely dependent on the content of N-dopants in graphene. Therefore, we assumed that N-doping in graphene is not sufficient to catalyze ORR. In other words, oxygen co-doping is essential to activate N-doped graphene for ORR activity. The ratios between N% and C-O% ranging from 0.2 for N30, 0.44 for Ar-N, 0.35 for O-N to

0.34 for Ar-O-N indicate that an optimal doping proportion between N and O dopants should lead to higher ORR performance in graphene.

We note that the characterization of chemical composition alone is not sufficient to reveal the effect of carbon vacancies induced by Ar plasma treatment on ORR. Therefore, we further elaborate the relationships of the ORR activities and structure of vacancy-containing graphene. As confirmed by the similar polarization behaviors of Ar-O vs Ar30 and O-Ar vs O10 (Figure 3c), the combination of vacancy defects and oxygen doping shows little cooperative effect for ORR. It shows that oxygen groups and vacancy defects play a similar role in activating ORR activity. Oxygen groups are however superior to vacancy defects. In contrast, the pre-doped vacancy defects generally improve the activities in graphene and N-doped graphene. For example, Ar30 has a lower ratio between atom % and ORR activity (9.3 atom % for 170 μ A) compared to G (9.9 atom % for 51 μ A) and N30 (10.1 atom % for 85 μ A), indicating the strong beneficial effect of vacancy defects on ORR. Moreover, N-doping in graphene containing oxygenated defects (Ar-O-N) is more active (390 μ A) than defect-free O-N (325 μ A). Overall, vacancy defects contribute to activate graphene with and without N doping for enhanced ORR activities.

A Koutecky-Levich (K-L) analysis was performed on the limiting currents for different graphene samples to confirm the activities and electron transfer number N_e (Figure 3g-i). The linear fits for the inverse of the limiting currents at 0 V vs RHE versus the inverse square root of the rotation rates in Figure 3g confirm the Koutecky-Levich behaviors. The intercepts of the K-L plots summarized in Figure 3i also reflect the catalytic capabilities of graphene samples, which are consistent with the summary of the activities in Figure 3f. Using the ring current I_r and disk current I_d collected from the RRDE data (see Figure S9), the electron transfer number N_e can be derived using equation (1)

$$N_e = 4I_d / (I_d + I_r/N) \quad (1)$$

where η is the current collection efficiency of the ring electrode (see Figure S11). The high ring currents for all the graphene samples indicate that hydrogen peroxide as the $2e^-$ product is still the main product. As shown in Figure 3h, N_e at various potentials for different graphene samples ranges from 2.5 to 3.5. Figure 3i further summarizes the averaged N_e in the potential range of -0.2 to 0.7 V. Ar30 exhibits the lowest N_e number of 2.5 while Ar-O and Ar-O-N shows the highest number of 3.4 to 3.5. Other samples display similar N_e numbers at the range of 2.8 to 2.9. Such contrasts in Ar30 versus Ar-O and Ar-O-N suggest that oxygenated defects can be the active sites responsible for water production while vacancy defects alone favor more hydrogen peroxide production. Given the similar N doping levels in Ar-N, O-N and Ar-O-N, as well as the similar N_e for Ar-O and Ar-O-N, it is concluded that nitrogen dopants should have little contribution to the $4e^-$ ORR pathway.

Taking both the effects of dopants and vacancy defects into consideration, it is hypothesized that oxygen dopants in the vicinity of vacancy defects in graphene act as the active sites for efficient $4e^-$ pathway,

while oxygen dopants is essential to activate N-doped graphene for ORR activity. The novel finding in this work is that the intentional or unintentional doped oxygen groups in the surface of monolayer graphene are the prerequisite for the N-doped carbon system with enhanced ORR activity. In brief, the pre-doped oxygenated defects create the activation center to integrate nitrogen heteroatoms for enhanced ORR activity and more efficient reduction towards water production. Nitrogen dopants contribute to optimize the electronic structure of the pre-doped graphene system. Moreover, the atom ratios of nitrogen versus oxygen dopants ($0.2 < \text{N\%/O\%} < 0.35$) are critical for achieving optimized ORR performance of doped graphene. On one aspect, our highlight for oxygen groups in N-doped graphene for ORR catalysis is also supported by a recent work identifying the $4e^-$ ORR active sites as sp^2 carbons that are located next to oxide regions in nitrogen-doped reduced graphene oxide.⁴⁴ In contrast, our work focuses on systematically disentangling the roles of potential elements involving carbon defects, oxygen and nitrogen dopants in contributing to the ORR reaction using a well-define graphitic surface of graphene. On another aspect, the contribution of nitrogen heteroatoms in pre-doped graphene for improved ORR activity in our work is partially in line with recent reports on defective carbon materials.^{19, 42} However, the oxygen contents that may intrinsically exist in the materials or unintentionally introduced during chemical processing are not taken into account in these previous reports. In contrary, our work constructively fills in the gap in understanding the critical roles of oxygen dopants for ORR in N-doped carbon systems with or without defects.

Specific roles of dopants and defects for ORR

An annealing treatment for Ar-O-N samples was performed to further confirm the critical contributions of oxygenation and vacancy defects to activating N-doped graphene for ORR. Figure 4a displays the LSV curves of Ar-O-N before and after 500 Celsius degree annealing (denoted as 500-Ar-O-N, see Methods for details) in comparison with Ar-O and Ar-N. It is evident that the annealing treatment significantly reduces the current of Ar-O-N to the levels between Ar-O and Ar-N, and decreases the onset potential to be similar with that of Ar-N (~ 0.57 to 0.59 V). The annealing treatment was expected to remove some functional groups in Ar-O-N samples and result in low defect density. Correspondingly, Raman spectra show that the defect density reflected by the $I(D)/I(G)$ ratio drop from 1.7 for Ar-O-N to 0.8 for 500-Ar-O-N (Figure 4b). Moreover, N 1s spectra of 500-Ar-O-N (Figure S10) shows the absence of N-dopants and an obvious rise in the atom % of sp^3 C comparing to Ar-O-N (from 9.4 to 14.9, Figure 4c and Table S2). Therefore, it is assumed that the decrease of defect density should be related to the removal of N-dopants. Moreover, the absence of nitrogen and the decreased activity in annealed samples supports the essential role of nitrogen dopants in graphene pre-doped with oxygenated defects for ORR. In addition, the increase of sp^3 C species could originate from the hydrocarbon contaminations during the annealing process rather than chemical functionalities in graphene surface considering the evident decrease in defect density. Importantly, the activity of 500-Ar-O-N correlates well with the sum contents of carbon-oxygen (C-O%) and nitrogen (N%) in comparison with other non-annealed samples (Figure 4d). Further Koutechy-Levich analysis in Figure 4e-f reveals that activities reflected by the K-L intercepts agree well with the current values in Figure 4d. For the electron transfer number N_e , 500-Ar-O-N exhibits the lowest number of 2.6,

lower than 2.8 for Ar-N and 3.3 for Ar-O (Figure 4f). As discussed above that oxygenated defects are most likely related to the $4e^-$ pathway, 500-Ar-O-N is expected to contain less active oxygenated defects due to atomic reconfiguration or contamination coverage induced by the annealing treatment.

Vacancy defects, oxygen and nitrogen dopants were doped in different orders into graphene to further evaluate their specific roles in activating ORR (Figure S12). Nitrogenation in graphene pre-doped with oxygenation and vacancy defects (Ar-O-N and O-Ar-N) still contribute to higher activities. In comparison, nitrogenation followed by oxygenation and vacancy introduction, namely N-Ar-O and N-O-Ar, contribute to relatively lower activities. Such contrasts confirm that oxygen and vacancy pre-doped graphene are more beneficial to improve the N-doping effect on ORR activity. The highest onset potential and electron transfer numbers are also found for Ar-O-N. As for the lower activity and onset potential for O-Ar-N than Ar-O-N, it is hypothesized that vacancy introduction after oxygenation may knock out the oxygen dopants, leaving fewer activation sites for N-doping. In brief, oxygenated defects predominate over other doping forms in activating nitrogen doping in graphene for ORR catalysis. These results further confirm that oxygenated defects are the critical active centers in carbon catalysts to integrate nitrogen dopants for enhanced ORR.

Conclusions

In summary, we used a well-defined monolayer graphene as a metal-free carbon catalyst to unveil the individual and synergy roles of nitrogen dopants, oxygen dopants and vacancy defects for ORR. Without the presence of oxygen dopants and vacancy defects, nitrogen doping alone in graphene results in low ORR activities. The presence of trace amounts of intrinsic oxygen groups on the surface of graphene leads to an enhanced activity upon nitrogen doping. The systematic incorporation of nitrogen into graphene pre-doped with oxygen dopants and vacancy defects further improves the ORR activity due to synergistic effects. Especially the presence of oxygenated defects demonstrates a significant boost in ORR activity in N-doped graphene. Further structure-activity correlations reveal that the sum atom ratios of oxygen and nitrogen dopants positively correlate to the enhanced ORR activity of doped graphene. Specifically, oxygenated vacancy defects in graphene act as an integrated center towards efficient $4e^-$ reduction and activated ORR activity, which can be further boosted by nitrogen dopants by modifying the electronic nature of the doped system. We believe that our findings provide new and critical insights in the understanding of the integrated active sites in complexed carbon systems and represent an important start for the rational design of highly efficient carbon catalysts.

Declarations

Data availability. The data that support the findings of this study are available from the corresponding author on request.

Acknowledgements

The research leading to this work has gratefully received funding from the Chinese Scholarship Council (L.J., 201406890016), the European Research Council (ERC starting grant 637556 Cu4Energy to D. G. H. H.), the European Research Council under the European Union's Seventh Framework Programme (FP/2007-2013) / ERC Grant Agreement n. 335879 project acronym 'Biographene', the Netherlands Organization for Scientific Research (Vidi 723.013.007). L.W. and J.P.H. acknowledge funding from the Netherlands Organization for Scientific Research (NWO) and co-financing by Shell Global Solutions International B.V. for the project 13CO2-6. L.J. appreciates Nicole W. G. Smits, Koen van der Ham and Michiel Langerman for helpful discussions.

Author contributions

L.J., G.F.S. and D.G.H.H. conceived and designed the experiments. L.J. performed all the sample preparations, characterizations and measurements. G.F.S., D.G.H.H. and M.T.M.K. supervised and coordinated the research. L.J. analyzed the data and constructed the discussion with the support of B.v.D. B.v.D. and D.G.H.H. provided the electrochemical instrument and contributed to the electrochemical experiments and analysis. L.W., C.M. and J.P.H. did the X-ray photoelectron spectroscopy characterizations and data analysis. V.T. provided the CVD graphene samples. L.J., B.v.D., G.F.S. and D.G.H.H. wrote the manuscript. All the authors discussed the results and commented on the manuscript.

References

1. Gong K, Du F, Xia Z, Durstock M, Dai L. Nitrogen-doped carbon nanotube arrays with high electrocatalytic activity for oxygen reduction. *Science* **323**, 760-764 (2009).
2. Shui J, Wang M, Du F, Dai L. N-doped carbon nanomaterials are durable catalysts for oxygen reduction reaction in acidic fuel cells. *Sci Adv* **1**, e1400129 (2015).
3. Ito Y, Qiu HJ, Fujita T, Tanabe Y, Tanigaki K, Chen M. Bicontinuous Nanoporous N-doped Graphene for the Oxygen Reduction Reaction. *Adv Mater* **26**, 4145-4150 (2014).
4. Qu L, Liu Y, Baek J-B, Dai L. Nitrogen-doped graphene as efficient metal-free electrocatalyst for oxygen reduction in fuel cells. *ACS Nano* **4**, 1321-1326 (2010).
5. Yang HB, *et al.* Identification of catalytic sites for oxygen reduction and oxygen evolution in N-doped graphene materials: Development of highly efficient metal-free bifunctional electrocatalyst. *Sci Adv* **2**, e1501122 (2016).
6. Lai L, *et al.* Exploration of the active center structure of nitrogen-doped graphene-based catalysts for oxygen reduction reaction. *Energy Environ Sci* **5**, 7936-7942 (2012).
7. Wang T, *et al.* Identifying the Active Site of N-Doped Graphene for Oxygen Reduction by Selective Chemical Modification. *ACS Energy Lett* **3**, 986-991 (2018).
8. Guo D, Shibuya R, Akiba C, Saji S, Kondo T, Nakamura J. Active sites of nitrogen-doped carbon materials for oxygen reduction reaction clarified using model catalysts. *Science* **351**, 361-365 (2016).

9. Wang N, *et al.* Graphitic nitrogen is responsible for oxygen electroreduction on nitrogen-doped carbons in alkaline electrolytes: insights from activity attenuation studies and theoretical calculations. *ACS Catal* **8**, 6827-6836 (2018).
10. Zheng Y, *et al.* Toward design of synergistically active carbon-based catalysts for electrocatalytic hydrogen evolution. *ACS Nano* **8**, 5290-5296 (2014).
11. Luo Z, *et al.* Pyridinic N doped graphene: synthesis, electronic structure, and electrocatalytic property. *J Mater Chem* **21**, 8038-8044 (2011).
12. Jia Y, *et al.* Defect graphene as a trifunctional catalyst for electrochemical reactions. *Adv Mater* **28**, 9532-9538 (2016).
13. Lu Z, *et al.* High-efficiency oxygen reduction to hydrogen peroxide catalysed by oxidized carbon materials. *Nat Catal* **1**, 156 (2018).
14. Kim HW, *et al.* Efficient hydrogen peroxide generation using reduced graphene oxide-based oxygen reduction electrocatalysts. *Nat Catal* **1**, 282 (2018).
15. Jia Y, *et al.* Identification of active sites for acidic oxygen reduction on carbon catalysts with and without nitrogen doping. *Nat Catal*, 1 (2019).
16. Li Q, Zhang S, Dai L, Li L-s. Nitrogen-doped colloidal graphene quantum dots and their size-dependent electrocatalytic activity for the oxygen reduction reaction. *J Am Chem Soc* **134**, 18932-18935 (2012).
17. Cote LJ, Kim F, Huang J. Langmuir-Blodgett assembly of graphite oxide single layers. *J Am Chem Soc* **131**, 1043-1049 (2008).
18. Zhang L, *et al.* Guiding Principles for Designing Highly Efficient Metal-Free Carbon Catalysts. *Adv Mater* **31**, 1805252 (2019).
19. Yan X, *et al.* Clarifying the Origin of Oxygen Reduction Activity in Heteroatom-Modified Defective Carbon. *Cell Reports Physical Science* **1**, 100083 (2020).
20. Radovic LR, Salgado-Casanova AJ. Hydrogen transfer and quinone/hydroquinone transitions in graphene-based materials. *Carbon* **126**, 443-451 (2018).
21. Belyaeva LA, Fu W, Arjmandi-Tash H, Schneider GgF. Molecular caging of graphene with cyclohexane: transfer and electrical transport. *ACS Cent Sci* **2**, 904-909 (2016).
22. Prydatko AV, Belyaeva LA, Jiang L, Lima LM, Schneider GF. Contact angle measurement of free-standing square-millimeter single-layer graphene. *Nat Commun* **9**, 4185 (2018).
23. Zhang L, Yu J, Yang M, Xie Q, Peng H, Liu Z. Janus graphene from asymmetric two-dimensional chemistry. *Nat Commun* **4**, 1443 (2013).
24. Ferrari AC, Basko DM. Raman spectroscopy as a versatile tool for studying the properties of graphene. *Nat Nanotechnol* **8**, 235-246 (2013).
25. Ferrari AC, Robertson J. Interpretation of Raman spectra of disordered and amorphous carbon. *Phys Rev B* **61**, 14095 (2000).

26. Eckmann A, Felten A, Verzhbitskiy I, Davey R, Casiraghi C. Raman study on defective graphene: Effect of the excitation energy, type, and amount of defects. *Phys Rev B* **88**, 035426 (2013).
27. Bruna M, Ott AK, Ijäs M, Yoon D, Sassi U, Ferrari AC. Doping dependence of the Raman spectrum of defected graphene. *ACS Nano* **8**, 7432-7441 (2014).
28. Das A, *et al.* Monitoring dopants by Raman scattering in an electrochemically top-gated graphene transistor. *Nat Nanotechnol* **3**, 210-215 (2008).
29. Wang QH, Shih C-J, Paulus GL, Strano MS. Evolution of physical and electronic structures of bilayer graphene upon chemical functionalization. *J Am Chem Soc* **135**, 18866-18875 (2013).
30. Lucchese MM, *et al.* Quantifying ion-induced defects and Raman relaxation length in graphene. *Carbon* **48**, 1592-1597 (2010).
31. Zafar Z, *et al.* Evolution of Raman spectra in nitrogen doped graphene. *Carbon* **61**, 57-62 (2013).
32. Eckmann A, *et al.* Probing the nature of defects in graphene by Raman spectroscopy. *Nano Lett* **12**, 3925-3930 (2012).
33. Jiang L, Fu W, Birdja YY, Koper MT, Schneider GF. Quantum and electrochemical interplays in hydrogenated graphene. *Nat Commun* **9**, 793 (2018).
34. Suk JW, *et al.* Transfer of CVD-grown monolayer graphene onto arbitrary substrates. *ACS Nano* **5**, 6916-6924 (2011).
35. Chen F, Qing Q, Xia J, Tao N. Graphene Field-Effect Transistors: Electrochemical Gating, Interfacial Capacitance, and Biosensing Applications. *Chem Asian J* **5**, 2144-2153 (2010).
36. Zhang C, Fu L, Liu N, Liu M, Wang Y, Liu Z. Synthesis of nitrogen-doped graphene using embedded carbon and nitrogen sources. *Adv Mater* **23**, 1020-1024 (2011).
37. Schiros T, *et al.* Connecting dopant bond type with electronic structure in N-doped graphene. *Nano Lett* **12**, 4025-4031 (2012).
38. Li J, *et al.* Electron-hole symmetry breaking in charge transport in nitrogen-doped graphene. *ACS Nano* **11**, 4641-4650 (2017).
39. Blizanac B, Ross P, Markovic N. Oxygen electroreduction on Ag (1 1 1): The pH effect. *Electrochim Acta* **52**, 2264-2271 (2007).
40. Sarapuu A, Helstein K, Vaik K, Schiffrin DJ, Tammeveski K. Electrocatalysis of oxygen reduction by quinones adsorbed on highly oriented pyrolytic graphite electrodes. *Electrochim Acta* **55**, 6376-6382 (2010).
41. Daems N, Sheng X, Vankelecom IF, Pescarmona PP. Metal-free doped carbon materials as electrocatalysts for the oxygen reduction reaction. *J Mater Chem A* **2**, 4085-4110 (2014).
42. Wang X, *et al.* A directional synthesis for topological defect in carbon. *Chem* **6**, 2009-2023 (2020).
43. Tang L, Ji R, Li X, Teng KS, Lau SP. Energy-level structure of nitrogen-doped graphene quantum dots. *J Mater Chem C* **1**, 4908-4915 (2013).
44. Kim HW, *et al.* Mechanisms of two-electron and four-electron electrochemical oxygen reduction reactions at nitrogen-doped reduced graphene oxide. *ACS Catal* **10**, 852-863 (2019).

Figures

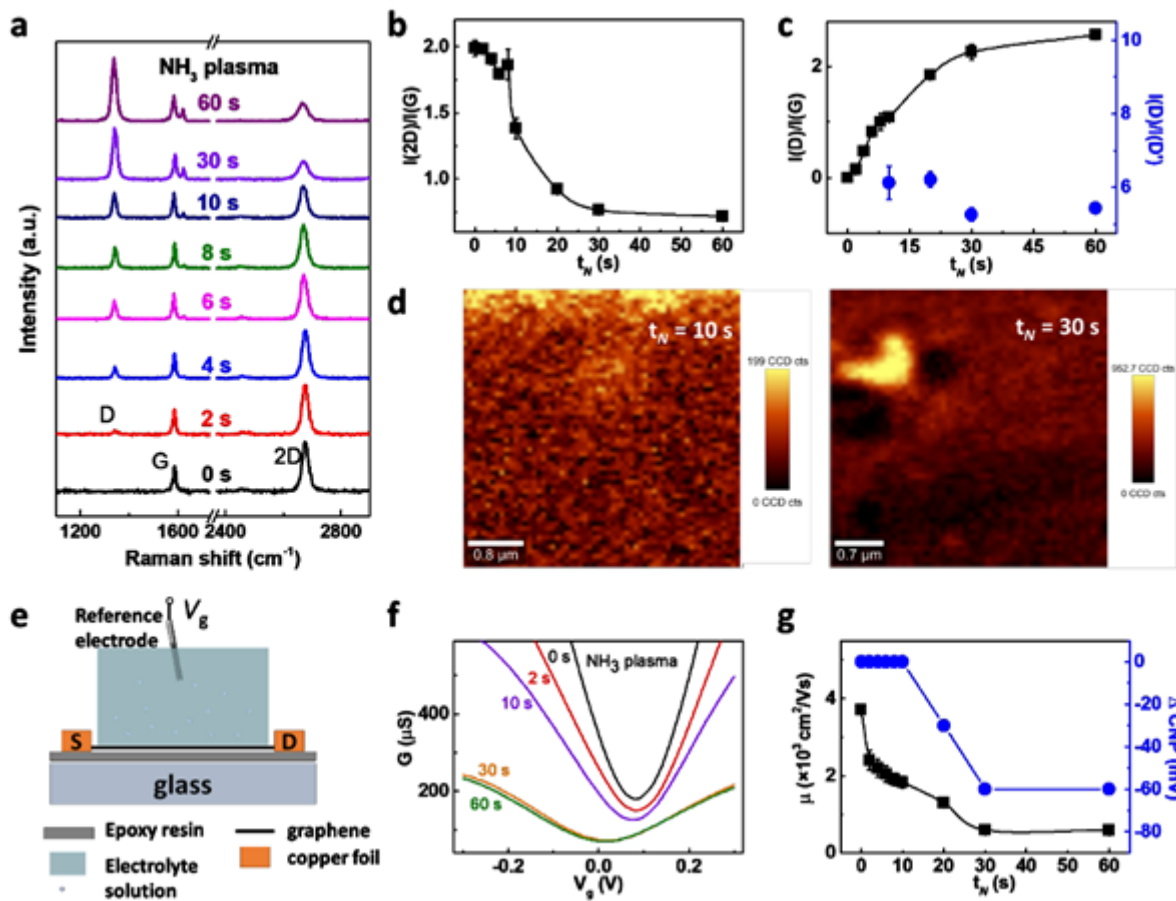


Figure 1

N-doping in monolayer graphene. (a) Raman spectra of graphene upon 0 to 60 s of nitrogenation using ammonia plasma. The spectra are recorded using 2.33 eV (532 nm) laser excitation. (b) Intensity ratio $I(2D)/I(G)$ as a function of nitrogenation times (t_N). (c) Evolution of intensity ratio $I(D)/I(G)$ (black) and $I(D)/I(D')$ (blue) with respect to nitrogenation times. (d) Raman mapping of the D band for graphene upon 10 s and 30 s of nitrogenation. (e) Scheme of a liquid-gated graphene field effect transistor (GFET). S: source electrode; D: drain electrode. The electrolyte solution is 0.1 M KCl with 10 mM Tris (pH 8). (f) Conductance (G) vs the gate voltage (V_g) curves of graphene upon t_N from 0 to 60 s. (g) The carrier mobility of graphene (μ , black square) and charge neutrality point (CNP, blue dot) evolve with the nitrogenated times t_N . The error bars in b, c, g are the standard deviation of experimental values

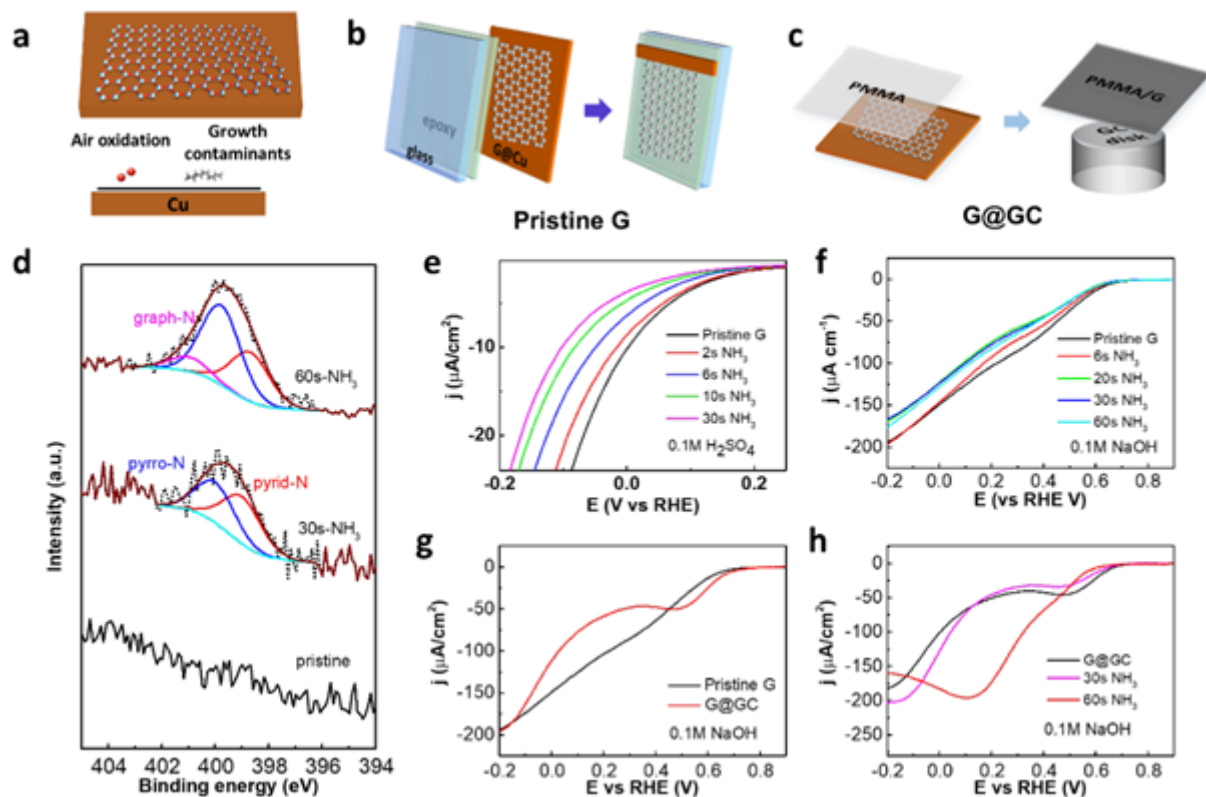


Figure 2

Graphene surface preparation for ORR. (a) Illustration of the asymmetrical surface of CVD graphene film: air-face and copper-face. (b) Preparation of pristine G supported by an epoxy substrate using the copper-face of graphene. (c) Preparation of G@GC using the air-face of graphene. (d) N1s core level spectra of pristine, 30 s and 60 s N-doped graphene. (e) Linear sweep voltammetry (LSV) polarization curves of graphene upon 0 to 30 s of nitrogenation in O₂-saturated 0.1 M H₂SO₄. (f) LSV curves of graphene upon 0 to 60 s of nitrogenation in O₂-saturated 0.1 M NaOH. (g) LSV curves of a pristine G and G@GC. (h) LSV curves of G@GC before and after 30 s, 60 s of nitrogenation.

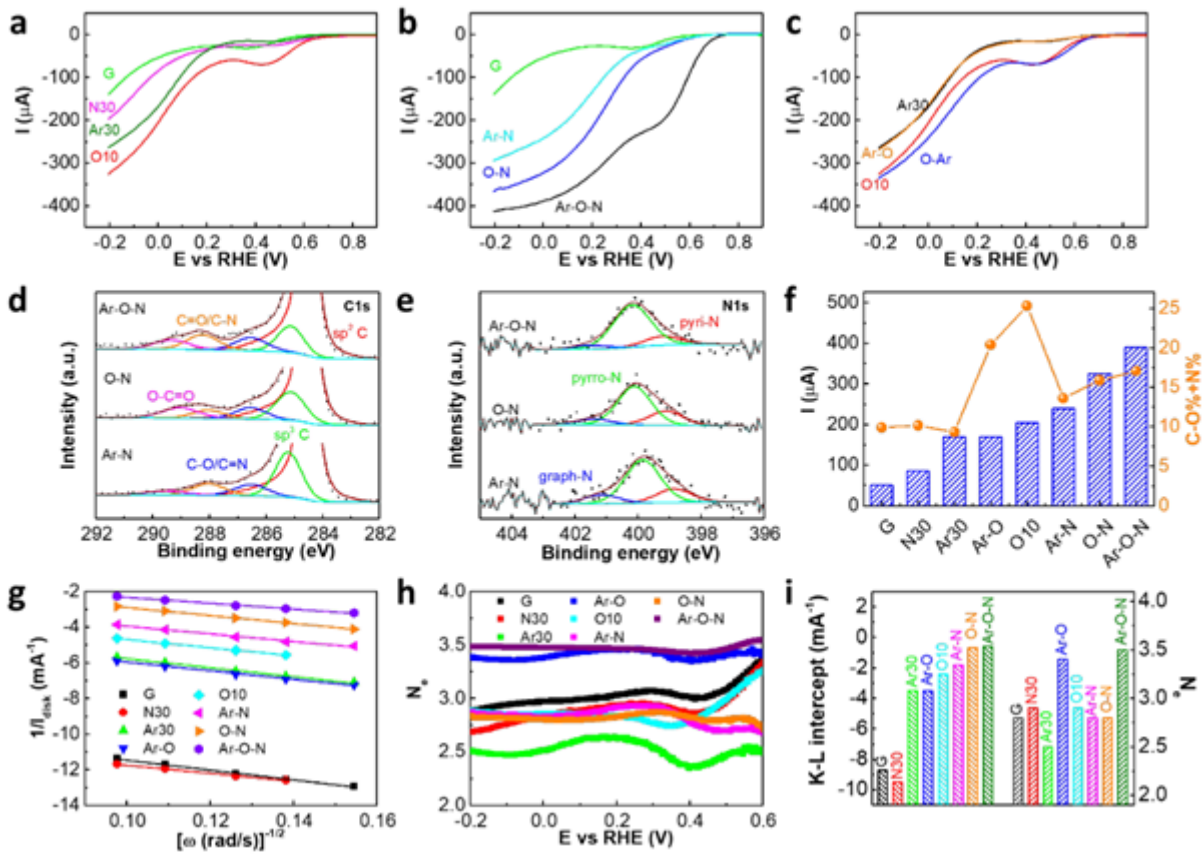


Figure 3

ORR activity correlates with chemical compositions on G@GC. a) LSV curves of G, N30, Ar30 and O10 samples at a rotation speed of 800 rpm. N30 represents 30 s nitrogenation, Ar30 for 30 s of argon plasma treatment, O10 for 10 s of oxygen plasma treatment. b) LSV curves of G, Ar-N, O-N and Ar-O-N samples. Ar-N represents graphene co-doped with Ar30 and N30, O-N for O10-N30, Ar-O-N for Ar30, O10 and N30 treated graphene. c) LSV curves of O-Ar and Ar-O in comparison to their mono-doping counterparts. d) C1s core level XPS spectra of Ar-N, O-N and Ar-O-N. e) N1s core level spectra of Ar-N, O-N and Ar-O-N. f) ORR activities correlate with atom % of carbon-oxygen and carbon-nitrogen (C-O%+N%) for non-, single- and dual-doped graphene samples. g) Koutecky-Levich (K-L) plots and linear fits of the inverse of the limiting currents at 0 V vs RHE for different doped graphene samples versus the inverse square root of the rotation rates. h) Electron transfer number N_e of different doped graphene samples at various potentials. i) K-L intercept extracted from panel (g) and N_e comparisons for different doped graphene. All the ORR experiments were performed in 0.1 M NaOH solutions saturated with O₂ at a rotation speed of 800 rpm (scan rate of 100 mV/s).

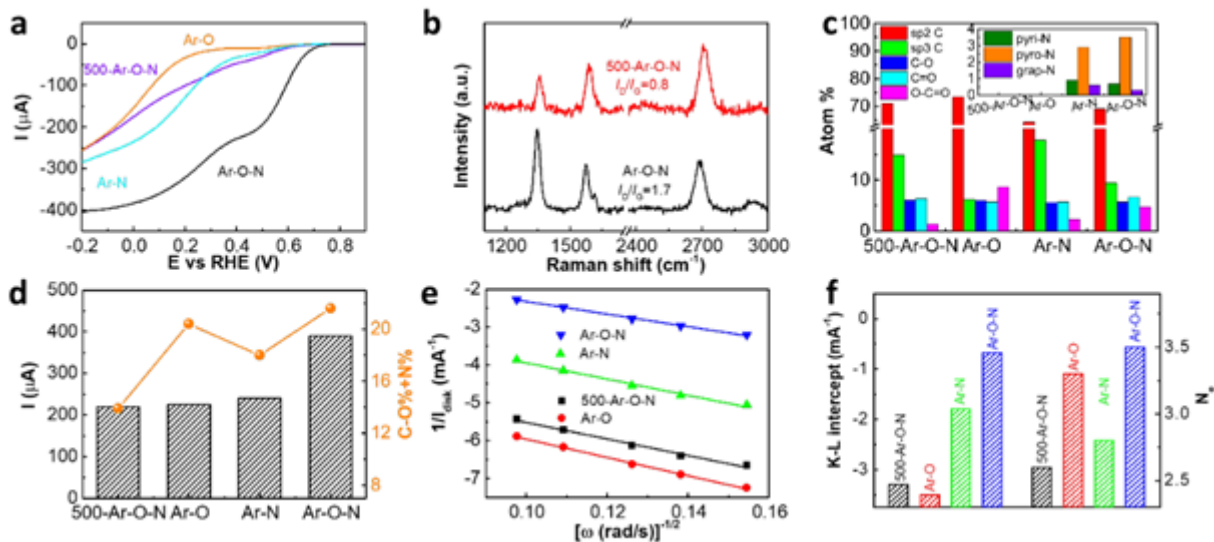


Figure 4

The specific roles of vacancy defects, oxygen and nitrogen dopants in ORR. a) LSV curves of Ar-O-N before and after annealing (500-Ar-O-N), Ar-O and Ar-N. b) Raman spectra of Ar-O-N and 500-Ar-O-N. c) Atom % comparisons of 500-Ar-O-N, Ar-O-N, Ar-O and Ar-N. d) Correlations of ORR activities with atomic % of carbon-oxygen and carbon-nitrogen (C-O%+N%) for 500-Ar-O-N, Ar-O-N, Ar-O and Ar-N. e) K-L plots of 500-Ar-O-N, Ar-O-N, Ar-O and Ar-N at 0 V. f) K-L intercept extracted from panel (d) and N_e comparison for 500-Ar-O-N, Ar-O-N, Ar-O and Ar-N. All the ORR experiments were performed in 0.1 M NaOH solutions saturated with O_2 at a rotation speed of 800 rpm (scan rate of 100 mV/s).

Supplementary Files

This is a list of supplementary files associated with this preprint. Click to download.

- [Sl.docx](#)